An Ultrathin Nanoporous Membrane Evaporator

An Ultra-Thin Nanoporous Membrane Evaporator

Zhengmao Lu[a], Kyle L. Wilke[a], Daniel J. Preston[a], Ikuya Kinefuchi[b], Elizabeth Chang-Davidson[a], Evelyn N. Wang[a*]

[a] Department of Mechanical Engineering, Massachusetts Institute of Technology, Cambridge, MA 02139, USA

[b] Department of Mechanical Engineering, University of Tokyo, Bunkyo, Tokyo 113-8656, Japan

* Corresponding author: enwang@mit.edu

Abstract

Evaporation is a ubiquitous phenomenon found in nature and widely used in industry. Yet fundamental understanding of interfacial transport during evaporation remains limited to date owing to the difficulty of characterizing the heat and mass transfer at the interface, especially at high heat fluxes (>100 W/cm^2). In this work, we elucidated evaporation into an air ambient with an ultra-thin (≈200 nm thick) nanoporous (≈130 nm pore diameter) membrane. With our evaporator design, we accurately monitored the temperature of the liquid-vapor interface, reduced the thermal-fluidic transport resistance and mitigated the clogging risk associated with contamination. At steady state, we demonstrated heat fluxes of ≈500 W/cm^2 across the interface over a total evaporation area of 0.20 mm^2. In the high flux regime, we showed the importance of convective transport caused by evaporation itself and that Fick's first law of diffusion no longer applies. This work improves our fundamental understanding of evaporation and paves the way for high flux phase-change devices.

Keywords: ultra-thin, nanoporous, evaporation, high flux, Maxwell-Stefan equation,

Evaporation is an effective cooling method widely utilized in nature (e.g., transpiration[1] and perspiration[2]) as well as for thermal management of electronic devices.[3, 4] It also plays a significant role in water desalination,[5] humidification,[6] and steam generation.[7] Previous studies[8-17] that attempted to characterize the heat and mass transfer at the interface level were generally limited to low interfacial heat fluxes ($\dot{q}''_{in} < 100$ W/cm^2) while it is desirable to have high heat fluxes in many applications.[3-5, 7]

When evaporation occurs in an air ambient, our traditional understanding is that without forced or natural convection, Fick's law of diffusion governs transport:

$$j = -D_v \nabla \rho \tag{1}$$

where j is the vapor mass flux, D_v is the binary diffusion coefficient of the air-vapor mixture and ρ is the vapor density. While Eq. (1) describes evaporation at low heat fluxes very well,[8, 9, 18] it does not apply to high flux cases as the bulk gas flow induced by evaporation becomes significant and in turn enhances the interfacial transport.

Theoretically, this has been reconciled by the Maxwell-Stefan equation[18] which accounts for convective transport. However, experimentally, it has been challenging to characterize the interfacial transport for this high flux case. First, the temperature of the liquid-vapor interface needs to be measured in an accurate and non-invasive way. When $\dot{q}''_{in}$ is high, this measurement becomes more difficult as the uncertainty in temperature measurement U_T can be estimated as

$$U_T = \dot{q}''_{in} \frac{\Delta L}{k} \tag{2}$$

where k is the thermal conductivity of the working fluid and ΔL is the uncertainty in where the temperature measurement is taken. For example, when $\dot{q}''_{in} = 100$ W/cm^2 and $k = 0.6$ W/m-K (for

water), then $\Delta L < 3$ μm is necessary for $U_T < 5$ °C, which has been difficult to achieve in previous work.[8-12, 19] Secondly, it is necessary to minimize the transport resistance associated with the heat supply, liquid refilling and vapor removal. Otherwise, it is not possible to reach a high flux across the interface. For example, Xiao et al. proposed a nanoporous configuration[20] for evaporation studies, where ΔL was reduced to the pore radius (≈75 nm), but their evaporative flux was still limited by the viscous loss in the refilling liquid flow along the pore due to the large pore length (>50 μm). Thirdly, the evaporation rate is very sensitive to contamination in the system. If the contaminants do not evaporate, the liquid-vapor interface accumulates the contaminants and eventually clogs the pores. Based on the 1-D diffusion-convection equation,[18] the steady state concentration of the contaminants at the interface c_i can be written as

$$c_i = c_b \exp\left(\frac{uL_{bi}}{D_c}\right) \tag{3}$$

where c_b is the concentration of such contaminants in the bulk working fluid, L_{bi} is the characteristic distance between the bulk fluid and the interface, u is the liquid flow velocity induced by evaporation, and D_c is the diffusion coefficient of the contaminant in the working fluid. According to Eq. (3), c_i scales exponentially with L_{bi} and therefore, a small L_{bi} helps maintain a relatively clean evaporating surface; this is especially important for the high flux regime where u becomes large.

In this work, we developed an ultra-thin, nanoporous membrane evaporator with a membrane thickness $t \approx 200$ nm and the pore radius $r \approx 65$ nm (see Supplemental Section I for the fabrication process flow). With this device, we were able to address all of the above challenges to experimentally investigate evaporation into an air ambient in the high flux regime. We fabricated a suspended membrane that connects two electrical contact pads, supported by the substrate

(Figure 1 (a)). The membrane includes a nanoporous area with porosity 0.23 (Figure 1 (b)), which is defined as the active region. The rest is the inactive region which is impermeable, generates no heating and thermally insulates the active part from the substrate. The active region is 0.26 mm × 3.4 mm in area, coated with Au which serves as both a resistive temperature detector (RTD) and a heater. This configuration allows us to measure the temperature very accurately, close to the interface since the distance between the RTD and the interface is at most r. It also minimizes the heat conduction resistance in the liquid phase (which scales with r) as well as the flow resistance along the pore (which scales with t) and mitigates the contamination risk ($L_{bi} = t$).[4, 21] This enables us to characterize the interfacial heat/mass transfer and demonstrate the importance of the convective transport induced by evaporation in the high flux regime.

During operation, liquid flows across the membrane and wicks into the nanopores, where it is resistively heated by the Au layer and evaporates into an air ambient (Figure 1 (c)). We set the input heating power and waited for the system to equilibrate at a certain temperature. Our system inherently contained a feedback loop. As we set the heating power to a higher value, the membrane temperature also increased, which gave rise to more intense evaporation and a higher cooling rate. When the cooling rate matched the heating power, the system reached a steady state. The response time of the system during the experiment was within one second due to the small thermal mass of the evaporator, and we maintained the steady state for five minutes before recording the data. The microfabricated samples of the same geometry (Sample 1-3) each were placed in a custom-designed test rig which is sealed to the air ambient and has a liquid feed-through and electrical connections (Figure 2 (a) and (b)). The inlet flow rate was maintained at 1 mL/min using a peristaltic pump, and deionized water was chosen as the working fluid. As our samples sit in the air ambient prior to the experiment for more than a day and water only partially wets gold that is

exposed to the laboratory air due to hydrocarbon adsorption,[22, 23] _ENREF_21 the working fluid does not flood the nanoporous membrane surface. A four-point measurement was utilized to monitor the resistance of the RTD and the power input to the heater. The RTD was calibrated to a T-type thermocouple prior to the experiment and the overall error of the temperature measurement in this study was 1.4 °C (see Supplemental Section II). Noting that evaporation is not the only heat dissipation mechanism in our system, we characterized the heat loss using a non-porous sample that has the same structure as Figure 1 (a) except that the active region is impermeable. The heating power Q_{loss} was determined to be proportional to the temperature rise of the sample ΔT with the proportionality constant $C = 4.50 \pm 0.03$ mW/°C (See Supplemental Section III for details). We then tested the ultra-thin nanoporous membrane evaporator with the same inlet flow rate (1 mL/min), heating the sample to induce evaporation while monitoring the membrane temperature T_s. The air ambient was quiescent at $T_\infty = 22.8$ °C and the relative humidity was 33%, such that the ambient water vapor density was $\rho_\infty = 0.00672$ kg/m^3. Therefore, the evaporative heat flux across the interface was calculated as

$$\dot{q}''_{\text{in}} = \frac{Q_{\text{J}} - Q_{\text{loss}}}{A_{\text{p}}} \tag{4}$$

where Q_{J} is the Joule heating power and A_{p} is the total pore area.

When the interfacial heat flux is low, Eq. (1) is used to model the evaporative transport. Based on energy conservation and the analogy between mass diffusion and heat conduction[24], we obtain from Eq. (1)

$$\dot{q}''_{in} = j_{\text{s}}\left(h_{\text{v}} - h_{\text{l}}\right) = \frac{D_{\text{v}}\left(\rho_{\text{s}} - \rho_{\infty}\right)}{A_{\text{p}} / S}\left(h_{\text{v}} - h_{\text{l}}\right) \tag{5}$$

where j_s is the mass flux across the interface, h_v is the enthalpy of vapor at the interface, h_l is the enthalpy of the liquid at the inlet, ρ_s is the saturated vapor density at the interface and S is the shape factor.[24] We designate $\delta = A_p/S$ which can be understood as the effective boundary layer thickness and is purely a geometric factor that scales generally with the characteristic length of the evaporator. D_v has a temperature dependence[18] and is evaluated at a reference temperature:[25]

$$T_{ref} = \frac{2}{3}T_s + \frac{1}{3}T_\infty. \tag{6}$$

In Figure 2 (c), we show $\dot{q}''_{in}$ as a function of $D_v(\rho_s - \rho_\infty)(h_v - h_l)$ which is the product of several temperature dependent properties. We fit the experimental data to a line, where δ^{-1} can be obtained from the slope based on Eq. (5) (δ = 12.8 μm).

Note that in Eq. (1), we did not consider the gravitational convection characterized by the Grashof number of the system

$$\mathrm{Gr} = \frac{g\Delta\rho_m\delta^3}{\rho_m\nu^2} \tag{7}$$

where g is the gravitational constant, ρ_m is the reference density of the air-vapor mixture, $\Delta\rho_m$ is the mixture density difference between the interface and the far field caused by the vapor concentration difference and the temperature difference, and ν is the kinematic viscosity of the mixture. Since Gr < 10^{-3} even for the highest interface temperature studied in this work, the gravitational convection is negligible.

Figure 3 (a) shows $\dot{q}''_{in}$ as a function of T_s. Using Fick's Law (Eq. (5), the blue dash line), the predictions, however, generally underestimates the interfacial heat flux in the experiments. This result indicates that the linear behavior observed in Figure 2 (c) was not maintained in the high

flux regime. On one hand, the water vapor concentration increases as T_s increases, such that the dilute-solution assumption of Fick's law no longer holds. Figure 3 (b) plots the relative deviation of the experimental data from the Fick's law prediction Δ_{Fick} as a function of the mass fraction of the vapor at the interface w_s, where Δ_{Fick} is generally less significant when w_s is smaller. On the other hand, the bulk flow of the vapor-air mixture can no longer be neglected as the evaporative flux increases. Figure 3 (c) plots Δ_{Fick} against the Péclet number of the system:

$$\mathrm{Pe} = \frac{V_m \delta}{D_v} \tag{8}$$

where V_m is the bulk velocity of the air-vapor mixture at the interface. Pe gives the ratio between the convective transport rate and the diffusive transport rate. Since Eq. (5) does not account for convection, Δ_{Fick} turns larger as Pe increases. Therefore instead of using Fick's law, we model the interfacial transport in the high flux regime with the Maxwell-Stefan equation[18] for this air-vapor diffusion problem:

$$j = -\rho_m D_v \nabla\left[-\ln\left(1-w_s\right)\right] \tag{9}$$

where ρ_m can be calculated as:[25]

$$\rho_m = \frac{2}{3}\rho_{m,s} + \frac{1}{3}\rho_{m,\infty}. \tag{10}$$

In Eq. (10), $\rho_{m,s}$ is the mixture density at the interface and $\rho_{m,\infty}$ is the mixture density in the far field. Eq. (9) utilizes the fact that the air is static and the pressure of air-vapor mixture is constant (at 1 atm), and it is not limited to small w_s and Pe.[18] Comparing Eq. (9) to Eq. (1), we can write the counterpart of Eq.(5):

$$\dot{q}''_{in} = \frac{D_v \rho_m \left(h_v - h_l\right)}{\delta} \ln\left(\frac{1-w_s}{1-w_\infty}\right) \tag{11}$$

where w_∞ is the mass fraction of the vapor in the far field. We use the same δ measured from Figure 2 (c) as it is only a geometric factor. We also plot Eq. (11) in Figure 3 (a) (pink solid curve), which agrees well with the experimental data over the whole range of interfacial fluxes. Indeed, Eq. (5) is just the limiting case of Eq. (11) and the enhanced convective transport further facilitates the interfacial heat/mass transfer in the high flux regime.

With the microfabricated ultra-thin nanoporous membrane evaporator, the present work shows that it is possible to reach high interfacial heat fluxes ($\approx$500 W/cm^2) with pure evaporation. This is realized by minimizing the thermal and fluidic resistance in the liquid phase and mitigate clogging risk from non-evaporative contaminants. Meanwhile, accurate measurement of the interface temperature is also achieved with this nanoporous configuration, which enables conclusive experimental investigation of evaporative transport. With our evaporation into air experiment, we experimentally demonstrate the validity of the Maxwell-Stefan equation when the interfacial heat flux is high. We note that the high flux evaporative transport was assisted by the small boundary layer thickness δ. If we scale up the system, this δ will become larger, which can increase the vapor diffusion resistance. With the present membrane evaporator as a research platform, future work on evaporation into pure vapor can be useful because the diffusion resistance will be eliminated regardless of the evaporator size, while the transport resistance in the liquid phase stays minimal. Overall, this ultra-thin nanoporous membrane evaporator facilitates the fundamental understanding of the interfacial transport and paves the way for further utilization of high flux evaporation in desalination, steam generation and thermal management.

We gratefully acknowledge funding support from the Air Force Office of Scientific Research with Dr. Ali Sayir as program manager.

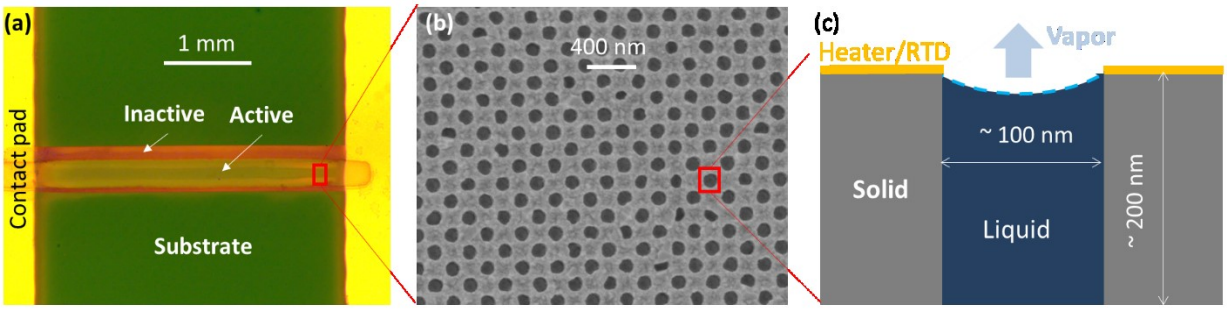

Figure 1 (a) Image of the fabricated ultra-thin nanoporous evaporator from an optical microscope: two Au contact pads are connected by a suspended membrane (~ 200 nm thick); the active part is nanoporous and coated with Au (≈ 40 nm thick) while the inactive part is impermeable and non-metallic. (b) Image of the nanopores patterned in the active part of the membrane from a scanning electron microscope. (c) Schematic of the cross-section of a nanopore (not to scale): evaporation is induced from a meniscus pinned at the top of the pore by resistively heating the Au layer.

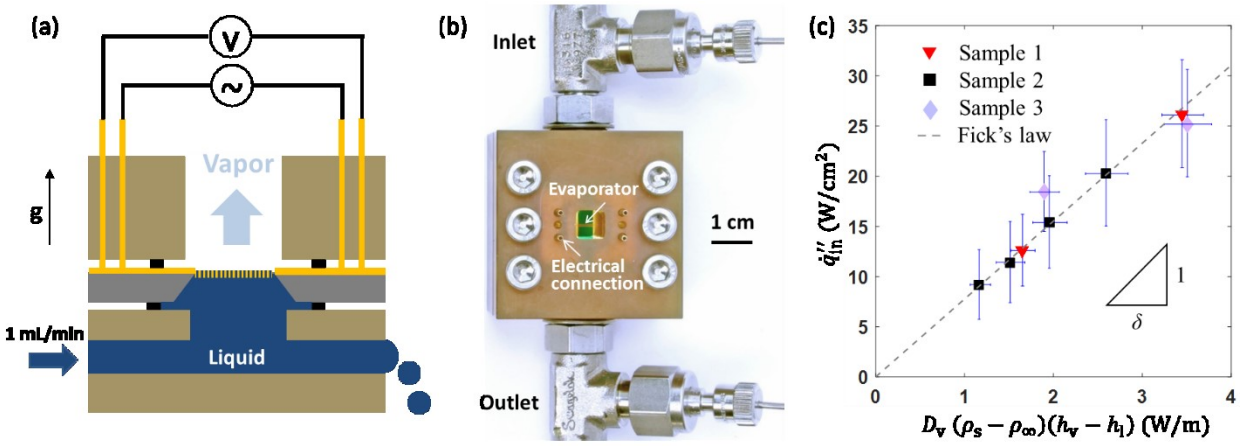

Figure 2 (a) Schematic of the experimental setup: the ultra-thin nanoporous evaporator is placed into a custom-designed test rig sealed to the ambient, facing downwards: DI water flows by the membrane at a constant flow rate (1 mL/min); heat is resistively applied to the Au layer to induce evaporation while the voltage and current is being monitored by a data acquisition system using a four-point measurement. (b) Image of the test rig with a liquid feed-through and electrical connections. (c) Measurement of the effective boundary layer thickness δ=12.8 μm at low evaporative fluxes: the heat flux averaged over the interface area $\dot{q}''_{in}$ is plotted against temperature dependent properties $D_v(\rho_s - \rho_\infty)(h_v - h_l)$. The red triangles, black squares and purple diamonds are the experimental data from Sample 1, Sample 2 and Sample 3 respectively. The gray dash line represents the results from the Fick's law (Eq. (5)) with δ as the fitting parameter.

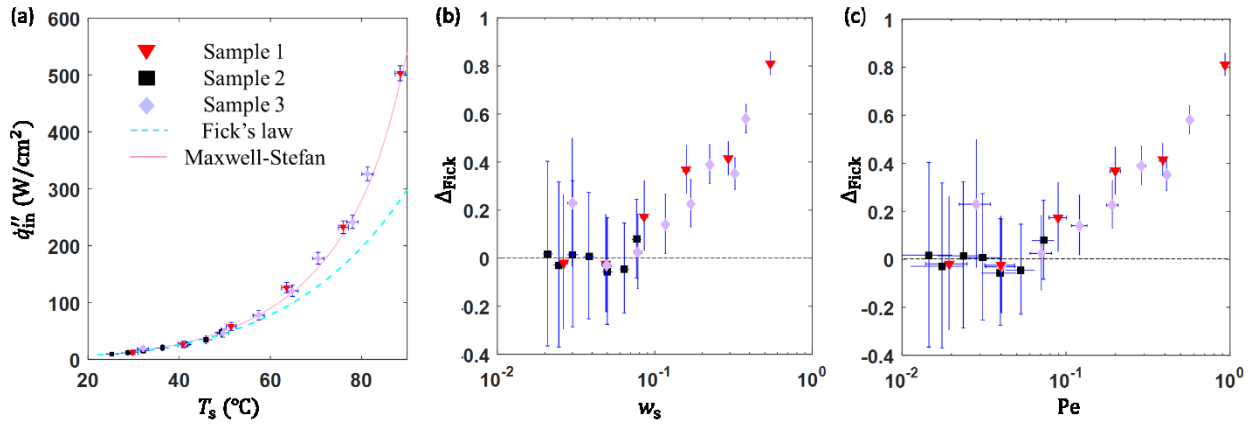

Figure 3 (a) The interfacial heat flux q''_{in} as a function of membrane temperature T_s over a large range of evaporative heat fluxes: the red triangles, black squares and purple diamonds are the experimental data from Sample 1, Sample 2 and Sample 3, respectively. The blue dash line and the pink solid line represent the model prediction from Fick's law and the Maxwell-Stefan equation, respectively, where both models use the same δ measured from Figure 2 (c). (b) Relative deviation from the Fick's law Δ_{Fick} vs the mass fraction of the water vapor at the interface w_s. (c) Relative deviation from the Fick's law Δ_{Fick} vs the Péclet number of the system Pe.

1. Sinha, R. K., *Modern plant physiology*. CRC Press: 2004.
2. Mosher, H. *J. Biol. Chem.* **1933,** 99, 781-790.
3. Faghri, A., *Heat pipe science and technology*. Global Digital Press: 1995.
4. Lu, Z.; Salamon, T. R.; Narayanan, S.; Bagnall, K. R.; Hanks, D. F.; Antao, D. S.; Barabadi, B.; Sircar, J.; Simon, M. E.; Wang, E. N. *IEEE Transactions on Components, Packaging and Manufacturing Technology* **2016,** 6, 1056-1065.
5. El-Dessouky, H. T.; Ettouney, H. *Desalination* **1999,** 125, 259-276.
6. Kabeel, A.; El-Said, E. M. *Desalination* **2014,** 341, 50-60.
7. Laing, D.; Bahl, C.; Bauer, T.; Lehmann, D.; Steinmann, W.-D. *Sol. Energy* **2011,** 85, 627-633.
8. Boelter, L.; Gordon, H.; Griffin, J. *Industrial & Engineering Chemistry* **1946,** 38, 596-600.
9. Kingdon, K. H. *Nature* **1965,** 206, 1148-1148.
10. Pauken, M. T. *Exp. Therm Fluid Sci.* **1998,** 18, 334-340.
11. Saylor, J.; Smith, G.; Flack, K. *Phys. Fluids* **2001,** 13, 428-439.
12. Ward, C.; Stanga, D. *Physical Review E* **2001,** 64, 051509.
13. Dhavaleswarapu, H. K.; Chamarthy, P.; Garimella, S. V.; Murthy, J. Y. *Phys. Fluids* **2007,** 19, 082103.
14. Dhavaleswarapu, H. K.; Garimella, S. V.; Murthy, J. Y. *J. Heat Transfer* **2009,** 131, 061501.
15. Ajaev, V. S.; Kabov, O. A. *Int. J. Heat Mass Transfer* **2017,** 108, 918-932.
16. Gatapova, E. Y.; Graur, I. A.; Kabov, O. A.; Aniskin, V. M.; Filipenko, M. A.; Sharipov, F.; Tadrist, L. *Int. J. Heat Mass Transfer* **2017,** 104, 800-812.
17. Kabov, O. A.; Zaitsev, D. V.; Kirichenko, D. P.; Ajaev, V. S. *Nanoscale Microscale Thermophys. Eng.* **2017,** 21, 60-69.
18. Bird, R. B.; Stewart, W. E.; Lightfoot, E. N., *Transport phenomena*. John Wiley & Sons: 2007.
19. Lu, Z.; Preston, D. J.; Antao, D. S.; Zhu, Y.; Wang, E. N. *Langmuir* **2017**.
20. Xiao, R.; Maroo, S. C.; Wang, E. N. *Appl. Phys. Lett.* **2013,** 102, 123103.
21. Lu, Z.; Narayanan, S.; Wang, E. N. *Langmuir* **2015,** 31, 9817-9824.
22. Gaines, G. L. *J. Colloid Interface Sci.* **1981,** 79, 295-295.
23. Preston, D. J.; Miljkovic, N.; Sack, J.; Enright, R.; Queeney, J.; Wang, E. N. *Appl. Phys. Lett.* **2014,** 105.
24. Lienhard, J. H., *A heat transfer textbook*. Courier Corporation: 2013.
25. Tonini, S.; Cossali, G. *Int. J. Heat Mass Transfer* **2016,** 92, 184-189.

TOC graphic

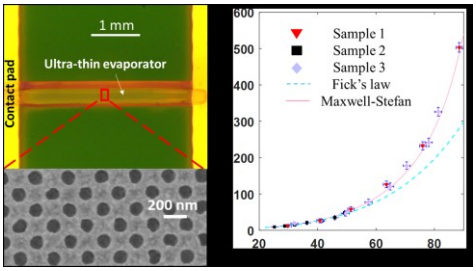
1 mm
Ultra-thin evaporator
Contact pad
200 nm
Sample 1
Sample 2
Sample 3
Fick's law
Maxwell-Stefan
600
500
400
300
200
100
0
20
40
60
80

Supplemental Information

An Ultrathin Nanoporous Membrane Evaporator

Zhengmao Lu[a], Kyle L. Wilke[a], Daniel J. Preston[a], Ikuya Kinefuchi[b], Elizabeth Chang-Davidson[a], Evelyn N. Wang[a*]

[a] Department of Mechanical Engineering, Massachusetts Institute of Technology, Cambridge, MA 02139, USA

[b] Department of Mechanical Engineering, University of Tokyo, Bunkyo, Tokyo 113-8656, Japan

*Corresponding author: enwang@mit.edu

I. Microfabrication Process

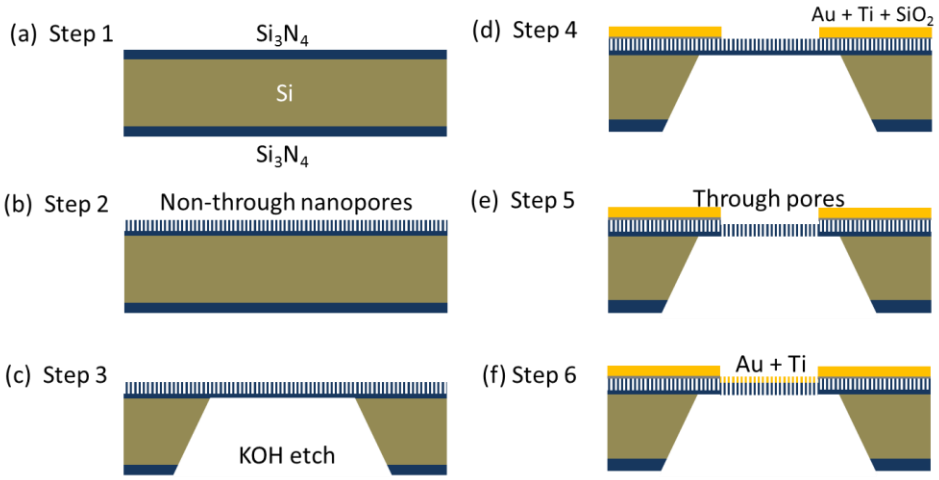

Figure S1 Schematic representation of the fabrication process: (a) Low pressure chemical vapor deposition of Si_3N_4. (b) Interference lithography that defines the nanopores and reactive ion etch that transfers the pattern partially into the Si_3N_4 layer. (c) KOH back etching with the front side Si is protected by the Si_3N_4 remaining from (b). (d) Contact pad deposition with shadow masking. (e) Nanopore through etching with shadow masking. (f) Heater/RTD deposition with the same mask alignment as (e).

Figure S1 shows the fabrication process of our device. Starting with a double side polished Si wafer (<100> orientation), we coated both sides with Si_3N_4 (~300 nm thick) using low pressure chemical vapor deposition in Step 1. Then, we used interference lithography to create nanoporous patterns on the front side and the pores were transferred into the front Si_3N_4 layer with reactive ion etching (RIE) in Step 2. During this step, the pores were not etched into the Si substrate. We then created a window with photolithography on the back side and used KOH etching to suspend the

front layer in Step 3 while the front side Si was protected by the Si_3N_4 remaining from the last step. After that, two Au contact pads were deposited using e-beam evaporation with shadow masking with SiO_2 as the insulation layer and Ti as the adhesive layer in Step 4. Using another shadow mask, we opened up the nanopores between the two contact pads with additional RIE in Step 5 and with the same mask alignment, we deposited a thin Au film with e-beam evaporation in Step 6.

II. Resistive Temperature Detector (RTD) Calibration

Prior to the experiment, the sample was placed in a box furnace (Thermo Scientific™ BF51766C-1), together with two thermocouples (Omega CPSS-116E-12) located close to it. We then set the furnace temperature with its own controller and waited for more than 2 hours for thermal equilibrium. The resistance of the sample R was measured using a four-point multimeter (Keithley 2001) and the temperature T_s was obtained from the thermocouples, shown in Figure S2.

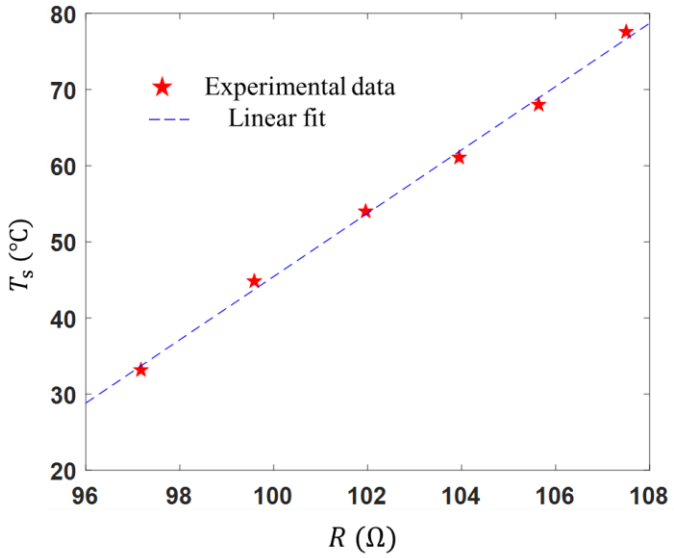

Figure S2 Temperature of the membrane evaporator vs its resistance: the experimental data (red pentagrams) are fitted to a linear model (blue dashed line).

We applied a linear fit to the experimental data and relied on this line to convert the RTD resistance to the temperature. The thermocouples from the manufacturer have an error of U_{tc} = 1.0 °C and the linear fit causes an additional error $U_{fit} \approx$ 1.0 °C. The overall error of the temperature measurement is given by $U_T = \sqrt{U_{tc}^2 + U_{fit}^2} \approx 1.4$°C.

III. Heat Loss Characterization

We characterized the heat loss using a non-porous sample that has the same structure as our membrane evaporator except that the active part is impermeable. Supplying the liquid at 1 mL/min, we resistively heated the sample which was cooled down by conduction and convection, resulting in a steady temperature rise of the sample from the ambient ΔT. In Figure S3, the heating power Q_{loss} is plotted as a function of ΔT. A linear fit was applied to the experimental data to obtain the heat loss conductance of the system C = 4.50 ± 0.03 mW/°C. The error originates from the conversion from the resistance change into the temperature rise (the slope in Figure S2 = 4.16 ± 0.31 °C/Ω).

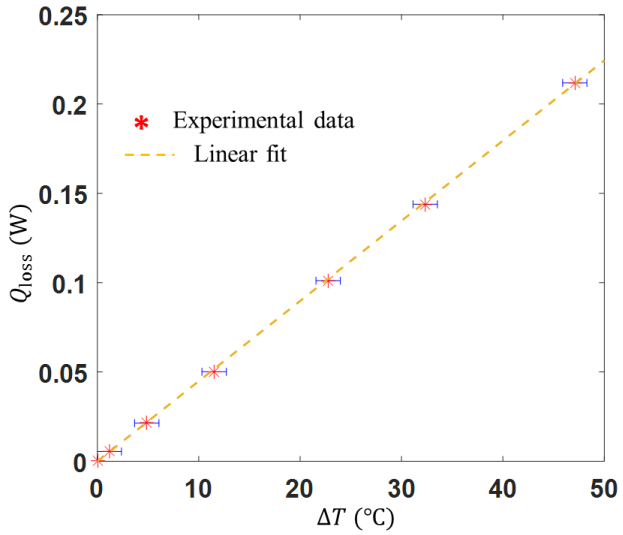

Figure S3 Heat loss of the system: a non-porous membrane with the same heater pattern was used. The heating power Q_{loss} is plotted against the temperature rise of the heater ΔT. The experimental data (red asterisks) were fit to a linear model (yellow dash line) $Q_{loss} = C\Delta T$, where C is the overall conductance for all of the heat loss mechanisms.